RAA 2014 Vol. **14** No. **8**, 959–970 doi: 10.1088/1674–4527/14/8/006
http://www.raa-journal.org *http://www.iop.org/journals/raa*

Research in Astronomy and Astrophysics

The comparison of H_2CO (1_{10}–1_{11}), $C^{18}O$ (1–0) and the continuum towards molecular clouds *

Xin-Di Tang[1,2], Jarken Esimbek[1,3], Jian-Jun Zhou[1,3], Gang Wu[1,2,3] and Daniel Okoh[1,4]

[1] Xinjiang Astronomical Observatory, Chinese Academy of Sciences, Urumqi 830011, China; *tangxindi@xao.ac.cn*
[2] University of Chinese Academy of Sciences, Beijing 100049, China
[3] Key Laboratory of Radio Astronomy, Chinese Academy of Sciences, Urumqi 830011, China
[4] Physics & Astronomy Department, University of Nigeria, Nsukka 410001, Nigeria

Received 2013 July 19; accepted 2014 February 20

Abstract We present large scale observations of $C^{18}O$ (1–0) towards four massive star forming regions: MON R2, S156, DR17/L906 and M17/M18. The transitions of H_2CO (1_{10}–1_{11}), $C^{18}O$ (1–0) and the 6 cm continuum are compared in these four regions. Our analysis of the observations and the results of the Non–LTE model shows that the brightness temperature of the formaldehyde absorption line is strongest in a background continuum temperature range of about 3 – 8 K. The excitation of the H_2CO absorption line is affected by strong background continuum emission. From a comparison of H_2CO and $C^{18}O$ maps, we found that the extent of H_2CO absorption is broader than that of $C^{18}O$ emission in the four regions. Except for the DR17 region, the maximum in H_2CO absorption is located at the same position as the $C^{18}O$ peak. A good correlation between intensities and widths of H_2CO absorption and $C^{18}O$ emission lines indicates that the H_2CO absorption line can trace the dense, warm regions of a molecular cloud. We find that $N(H_2CO)$ is well correlated with $N(C^{18}O)$ in the four regions and that the average ratio of column densities is $\langle N(H_2CO)/N(C^{18}O)\rangle \sim 0.03$.

Key words: ISM: clouds — molecules — stars: formation

1 INTRODUCTION

Dense molecular cloud cores are considered to be sites of star formation. Studying the structure and properties of these cores allows us to have a better understanding of the whole process of star formation. It is important to have a comprehensive understanding of the evolution of dense regions.

The first detection of H_2CO was reported by Snyder et al. (1969), which was the first organic polyatomic molecule discovered in the interstellar medium. The dense clumps in the line of sight may be regions of H_2CO production (Prasad & Huntress 1980). Formaldehyde absorption provides a powerful tool for analyzing the distribution of dense interstellar gas (Scoville et al. 1972). For typical densities of clouds near HII regions (10^3 to 10^5 cm^{-3}) the 1_{10}–1_{11} transition of H_2CO is ideal for identifying motions (Gardner et al. 1984). The 4.83 GHz 1_{10}–1_{11} transition of interstellar H_2CO

* Supported by the National Natural Science Foundation of China.

is easily observed in absorption against a Galactic continuum source. In addition, it is easily seen in absorption toward many dark clouds, where the molecule's lines absorb the cosmic microwave background (CMB) radiation.

Downes et al. (1980) found that the intensity of a H_2CO absorption line is strongly affected by the background continuum emission in the HII region. Zhang et al. (2012) obtained a similar result in giant molecular clouds, and inferred that the contribution of CMB radiation to the H_2CO intensity was very weak. Giant HII regions have many compact components that radiate in the continuum, and the absorption by H_2CO is affected by the distribution of these components. A study mapping 12 bright Galactic HII regions and two dark clouds showed that areas with strong H_2CO absorption were quite far away from the bright continuum peaks in a number of cases (Bieging et al. 1982). Pipenbrink & Wendker (1988) surveyed the brightest features in the Cyg X region and found that there are 22 positions where no H_2CO absorption line was detected. This is especially surprising given the high brightness levels of HII regions.

Recently, Tang et al. (2013) studied the correlation among H_2CO (1_{10}–1_{11}), ^{12}CO (1–0) and ^{13}CO (1–0) towards the MON R2, S156, DR17/L906 and M17/M18 regions, and they found that integrated intensity maps of H_2CO and ^{13}CO had analogous shapes, sizes, peak positions and molecular spectra, presenting similar central velocities and line widths. Such a good agreement indicates that the H_2CO absorption and the ^{13}CO emission lines arise from similar regions. The ^{12}CO (1–0) line was not suitable for tracing the star forming region because of the larger optical depth. The ^{13}CO (1–0) spectra tended to be saturated towards the high density regions, making it difficult to understand the detailed distribution of high density regions. The abundance of $C^{18}O$ molecules is less than that of the ^{13}CO molecules by a factor of $\sim$5. The $C^{18}O$ line is optically thin compared to ^{13}CO and it can be used to trace dense regions ($> 10^4$ cm^{-3}) (Dame et al. 1986). Therefore, $C^{18}O$ is a good spectral line to trace dense regions in nearby star forming regions. Minn et al. (1996) have compared the distributions of the H_2CO 6-cm absorption and $C^{18}O$ (1–0) emission (Fuller et al. 1991) towards the region of dark cloud B5. They found that the two molecular lines showed a similar spatial distribution with both peaks at the same position. One thing that H_2CO and $C^{18}O$ have in common is that they have both been used as probes to trace dense gas. The 1_{10}–1_{11} transition of H_2CO is a unique probe that can trace high-density gases in low temperature regions. Liszt & Lucas (1995) and Liszt et al. (2006) have found that $N(H_2CO)$ is quite well correlated with $N(HCO^+)$, $N(C_2H)$, $N(HCN)$, $N(CS)$ and $N(NH_3)$ in diffuse clouds. Toward the cold, dense pre-protostellar cores, H_2CO is depleted (Young et al. 2004). Therefore, H_2CO will show different properties towards the warm, high-density regions.

In this paper, we present a comparison of H_2CO, $C^{18}O$ and the continuum on a scale of $2 \sim 10$ pc towards four Galactic HII regions: MON R2, S156, DR17/L906 and M17/M18. We are interested in two issues: (1) to seek the relationship between the H_2CO line and the background continuum; and (2) to make a comparative study of the H_2CO and $C^{18}O$ lines.

In Sections 2 and 3 we describe the observations and results. In Section 4 we discuss a comparison of results among H_2CO, $C^{18}O$ and the continuum. A summary is provided in Section 5. The Non-LTE model for H_2CO calculations is given in the Appendix (see online version).

2 OBSERVATIONS

The ^{12}CO, ^{13}CO and $C^{18}O$ observations in the four regions of MON R2 ($60' \times 90'$), S156 ($50' \times 70'$), DR17/L906 ($40' \times 60'$) and M17/M18 ($70' \times 80'$) have been carried out at the 13.7 m radio telescope administered by Purple Mountain Observatory in Delingha from 2011 May 15 to 26, and the ^{12}CO and ^{13}CO data were reported in Tang et al. (2013). The HPBW was $60''$ at 110 GHz and the beam efficiency was 48%. A Fast Fourier Transform Spectrometer was used, and the three CO lines were observed simultaneously. The velocity resolution of ^{12}CO was 0.16 km s^{-1} while the velocity resolution of ^{13}CO and $C^{18}O$ was 0.17 km s^{-1}. The observation was performed in the On-

The-Fly mode. The average integration time of every point was one minute. H_2CO and continuum data were selected from Tang et al. (2013). Four HII regions were observed at the 1_{10}–1_{11} transition of H_2CO and the 4.8 GHz continuum by Tang et al. (2013) using the Nanshan 25 m radio telescope administered by Xinjiang Astronomical Observatory.

3 RESULTS

3.1 Data Reduction and Distribution

$C^{18}O$ data were reduced using CLASS and GREG, which are parts of the GILDAS software developed by IRAM[1]. CLASS was used to remove baselines, average the weighted spectra, and to calibrate the data. The line-center velocities ($V_{\rm LSR}$) and line width (ΔV) were determined by fitting Gaussian profiles to the spectral lines. For comparison between $C^{18}O$ and H_2CO data, we have smoothed the $C^{18}O$ observations to $10'$, and resampled them on a H_2CO observing grid. GREG was used to map the $C^{18}O$ data.

Towards the four regions under study, we map the integrated intensity of the $C^{18}O$ emission in Figure 1 and the $C^{18}O$ line spectra are shown in Figure 2. The parameters $C^{18}O$ are listed in Table B.1 (see online version). The optical depth and column density of $C^{18}O$ were estimated following calculations from Sato et al. (1994), on the assumption that the cloud is in Local Thermodynamic Equilibrium (LTE) and the excitation temperature of $C^{18}O$ is the same as that of ^{12}CO. Estimations of the peak optical depth and column density for H_2CO were done following Pipenbrink & Wendker (1988), using the result of a simple standard radiative transfer.

3.2 Description of Sources

MON R2. – The Mon R2 association of reflection nebulae (van den Bergh 1966; Racine 1968) is a nearby star forming region that shows complex structure and is about 830 pc from the Sun (Herbst & Racine 1976). The molecular content of this region has been the subject of several observational studies over the last several decades. Continuum observations at 6 cm have been reported by Wood & Churchwell (1989), which showed that the associated ultracompact HII region is highly asymmetric and reaches its maximum brightness toward its exciting star Mon R2 IRS1. Downes et al. (1975) found the existence of OH maser emission, as well as H_2CO and OH absorption in this region. Using the ^{13}CO and $C^{18}O$ maps, the mass of molecular gas in the Mon R2 core was determined by Ridge et al. (2003). The $C^{18}O$ result shows a gas mass of 1826 $M_\odot$, while the more abundant ^{13}CO gives a mass of 2550 $M_\odot$.

Maps of the integrated intensities of the $C^{18}O$ line velocities range from 0 to 20 km s^{-1} in Figure 1(a). The spectrum of intensity peaks for $C^{18}O$ shows velocity components at 10.4 km s^{-1}, which agrees with values of velocity components associated with H_2CO lines at 10.5 km s^{-1}. Owing to its weakness, the H110α recombination line was not detected by Tang et al. (2013). The formation of massive stars in this region is occurring on the back side of the cloud (Gilmore 1980). It also could be that the foreground gas and dust are blocking the H110α recombination line. A good agreement between the H_2CO and the continuum distributions (see fig. A.5(a), Tang et al. 2013) suggests that the continuum emission comes from the HII region and that the H_2CO absorbs the background continuum.

S156. –S156, also known as IC 1470, is a compact HII region associated with an extensive molecular cloud lying in the direction of the Perseus arm. The 6-cm H_2CO absorption and OH emission have been observed by Hoglund & Gordon (1973) in this region, who found a general correlation among HI absorption, H_2CO absorption and OH emission. High resolution continuum

[1] The GILDAS package was developed by the Institute de Radioastronomie Millimétrique (IRAM). *http://www.iram.fr/IRAMFR/GILDAS.*

observations at 6 cm toward the S156 HII region have been reported by Israel (1977). Its distance is $\sim 3.5 - 4.3$ kpc from the Sun (Hoglund & Gordon 1973).

The integrated intensities of the line velocities of $C^{18}O$ maps range from -55 to -45 km s^{-1} in Figure 1(b). The spectrum of intensity peaks of $C^{18}O$ illustrates velocity components at -52.1 km s^{-1}, which agree with those of H_2CO at -50.2 km s^{-1}. The H110α recombination line was not detected (Tang et al. 2013). The strong absorption extends well outside the continuum source, and is absent in front of weaker continuum emission to the north and south of the main continuum source (see fig. A.5(b), Tang et al. 2013). The wider H_2CO line width in the central part of the cloud shows that the cloud could be affected by the HII region (Tang et al. 2013). Therefore, the H_2CO absorption may not absorb the background continuum.

DR17/L906. – DR17 is an extended HII region with an arc of mid-IR emission associated with the molecular clouds in Cygnus X-North (Schneider et al. 2006). A high resolution continuum in the 6-cm survey of the Cygnus X region has been presented by Wendker (1984). The H110α and H_2CO at 6-cm have been reported by Pipenbrink & Wendker (1988). The distance is about 0.8 kpc from the Sun. The source at the southern tip of DR17 is L906, which is a small dark cloud (Davis et al. 2007).

Maps of the integrated intensities of the $C^{18}O$ line velocities range from –10 to 20 km s^{-1} in Figure 1(c). The $C^{18}O$ line was not detected towards the DR17 HII region. The $C^{18}O$ velocity components at 14.4 km s^{-1} and the H_2CO velocity component at 15.4 km s^{-1} are associated with the L906 region. The strong H110α emission was detected in the DR17 region by Tang et al. (2013). H110α is coincident with the south continuum source, and the H_2CO distributions show good agreement with the continuum distribution (see fig. A.5(c), Tang et al. 2013). Therefore, H_2CO absorbs the continuum that comes from the DR17 HII region. The agreement between the continuum and H_2CO distributions in the L906 region is not better than that of the DR17 region, and the H110α and the continuum emission are both weak. H_2CO may absorb the background continuum in the L906 region.

Towards the DR17 region, the cloud shows a large area of H110α emission (see fig. A.5(c), Tang et al. 2013). This implies that there could be a strong source of UV radiation in the DR17 region. 2MASS images have recognized two OB clusters [LK 2002]Cl-12 ([DB 2001]Cl-15) that could be exciting sources for the HII region and the mid-IR loop emission (Schneider et al. 2006). The molecular cloud could be eroded by the strong background radiation field, stellar wind or ionized gas in the DR17 HII region. So, this gives a comparison between the lower abundance of H_2 in the DR17 HII region and the L906 region. Generally, the intensity of an absorption line from H_2CO depends on the background continuum temperature and the gas density, so it would be strong where the background continuum is strong, although the gas density is lower. Only one H_2CO peak is associated with continuum emission in the DR17 region. In comparison to the H_2CO peaks in the DR17 region, there are weak continuum and H110α emissions associated with H_2CO peaks in the L906 region; however, the intensity of H_2CO is similar in these two regions. The DR17 region has a stronger continuum temperature and lower $n(H_2)$ density, but there are weaker continuum emissions and higher $n(H_2)$ densities are in the L906 region. Therefore, the reason for similar H_2CO intensities in the DR17 and L906 regions may be that the different continuum temperatures and different gas densities together influence the intensities of the H_2CO absorption line.

M17/M18. – M17 features a visible HII region, which is one of the youngest, most massive nearby star forming regions in the Galaxy (Povich et al. 2009). Observations of 6-cm H_2CO toward the M17 region have been done by Lada & Chaisson (1975) and Bieging et al. (1982). The continuum radiation of M17 was mapped at a wavelength of 6 cm by Mezger & Henderson (1967). The distance is about 1.5 kpc from the Sun (Downes et al. 1980). M18 is a young open cluster in Sagittarius (Lindoff 1971; McSwain & Gies 2005). It is about 1.25 kpc from the Sun (Lindoff 1971). There are hundreds of dark clouds in the regions associated with M17/M18.

The integrated intensities of the line velocities from $C^{18}O$ maps range from 10 to 50 km s^{-1} in Figure 1(d). The spectrum of intensity peaks from $C^{18}O$ shows velocity components at 20.0 km s^{-1},

which agrees with the velocity components from H_2CO lines at 22.2 km s^{-1}. Strong H110α and continuum emissions were detected in the M17 region (Tang et al. 2013), and there was a good agreement between them. There is a deviation of about 10′ (~ 4 pc) between H_2CO intensity, H110α and the continuum peaks in the direction of M17 (see fig. A.5(d), Tang et al. 2013). The H_2CO absorbs the continuum that comes from the M17 HII region, despite there being an offset. At the same time, the peaks of the ^{12}CO (1–0), ^{13}CO (1–0) and $C^{18}O$ (1–0) intensities are associated with H_2CO peaks (see fig. 2(d) and figs. A.1(d) and A.3(d) in Tang et al. 2013). The M17 HII region erupts from the side of the giant molecular cloud M17 SW (Lada 1976). Tsivilev & Krasnov (1999) and Pellegrini et al. (2007) have shown that the entire HII region in the M17 region is expanding, and the HII region is eroding the M17 molecular cloud. This may happen because the strong radiation field coming from the M17 HII region has ionized the molecular cloud and affected the distribution of the giant molecular cloud. This could be a reason for the offset between the H_2CO intensity and continuum peaks.

4 DISCUSSION

4.1 Comparison between H_2CO and Background Continuum

The relationship between H_2CO line temperatures and continuum temperatures has been noted by Zhang et al. (2012) in four HII regions. They concluded that the integrated intensity of H_2CO is positively correlated with the background continuum temperature when the continuum temperature is below 6 K. These regions, as well as the four regions observed by Tang et al. (2013), have a low range of continuum temperatures ($T_C < 10$ K), thus it is difficult to understand how the intensity of H_2CO varies in a region of the continuum with high brightness. Consequently, we have selected some sources (including giant molecular clouds (GMCs) and HII sources) from the previous observations of H_2CO and continuum, and plotted these sources together in Figure 3. The intensity of an absorption line is proportional to intensity of the background continuum because intensity of the continuum is below about 10 K, which agrees with the conclusion of Zhang et al. (2012). Above this value, the intensity of an H_2CO line shows a slight dispersion and may weakly correlate with the background continuum intensity. This suggests that the H_2CO intensity is strongly influenced by the strong background continuum emission. Actually, although the intensity of H_2CO absorption lines depends on the background continuum level, they also depend on H_2CO column density and gas density (e.g., Garrison et al. 1975; Wootten et al. 1980).

We compared results from the Non–LTE interstellar line spectra model (van der Tak et al. 2007) with the observed results. The Non–LTE model shows a similar distribution of the relation between the H_2CO line intensity and the background continuum intensity (see Fig. A.1). The intensity of absorption lines is proportional to the background continuum intensity, which guarantees a rough proportionality between the 6 cm continuum and the H_2CO intensity until the 6 cm continuum reaches some critical values corresponding to a background continuum brightness of about 3 – 8 K. Above this critical value, the intensity of the H_2CO line decreases as the background continuum temperature increases. Under this condition where the H_2CO cloud has a field with strong background continuum emission, the H_2CO cloud can also be heated, so part of the H_2CO cloud could be thermalized. The excitation temperature of the H_2CO absorption lines would increase above 2.7 K. This suggests that the strong background continuum emission affects the excitation of the H_2CO absorption line. This could be a reason why strong H_2CO absorption occurred quite far away from bright continuum peaks in some clouds.

The statistics describing observed results indicate that approximately 75% of observed positions with the line-to-continuum ratio $|T_L/T_C|$ are less than 0.2 and the average value $\langle|T_L/T_C|\rangle$ is about 0.066, which is higher than the value of 0.052 estimated by Whiteoak & Gardner (1974) for 280 Galactic radio sources or source components. Towards the regions of MON R2, S156 and L906, the $|T_L/T_C|$ ratios are higher than those towards the HII regions associated with DR17 and M17.

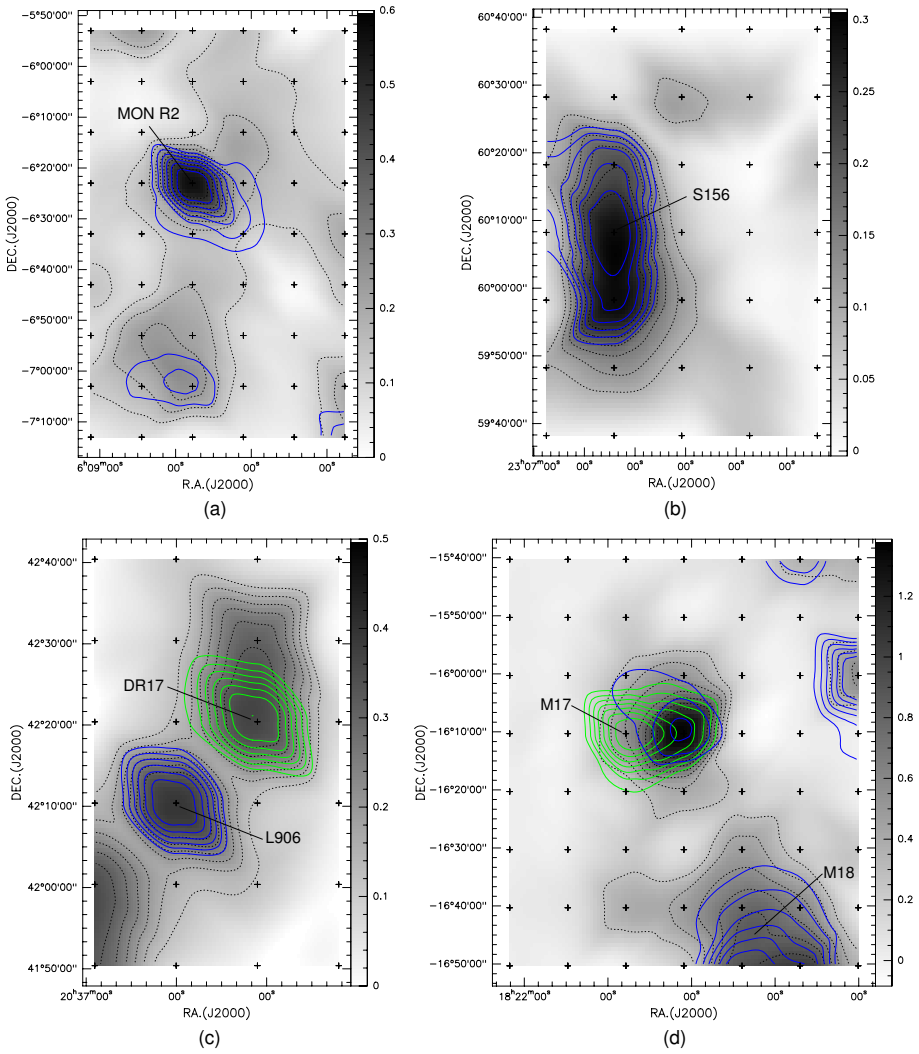

Fig. 1 Contour maps of integrated area toward (a) MON R2, (b) S156, (c) DR17/L906 and (d) M17/M18. The black contours, green contours and blue contours, respectively, indicate the integrated intensity of the H_2CO absorption line, H110α recombination line and $C^{18}O$ emission line. H_2CO and H110α data were selected from Tang et al. (2013). (a) For the MON R2 region, $C^{18}O$ contour levels are 0.20 to 0.66 in steps of 0.06 K km s^{-1}. (b) For the S156 region, $C^{18}O$ contour levels are 0.20 to 0.46 in steps of 0.05 K km s^{-1}. (c) For the DR17/L906 region, $C^{18}O$ contour levels are 0.22 to 0.49 in steps of 0.05 K km s^{-1}. (d) For the M17/M18 region, $C^{18}O$ contour levels are 0.80 to 2.12 in steps of 0.27 K km s^{-1}. The gray bars are given in units of K km s^{-1} for the negative integrated intensity of H_2CO.

Tang et al. (2013) detected strong H110α and continuum emission in the regions of DR17 and M17, but did not detect H110α emissions towards the regions of MON R2, S156 and L906, which have weak continuum emission. It is suggested that the presence of strong H110α and 6 cm continuum emissions is the reason why high $|T_L/T_C|$ ratios do not occur in these regions.

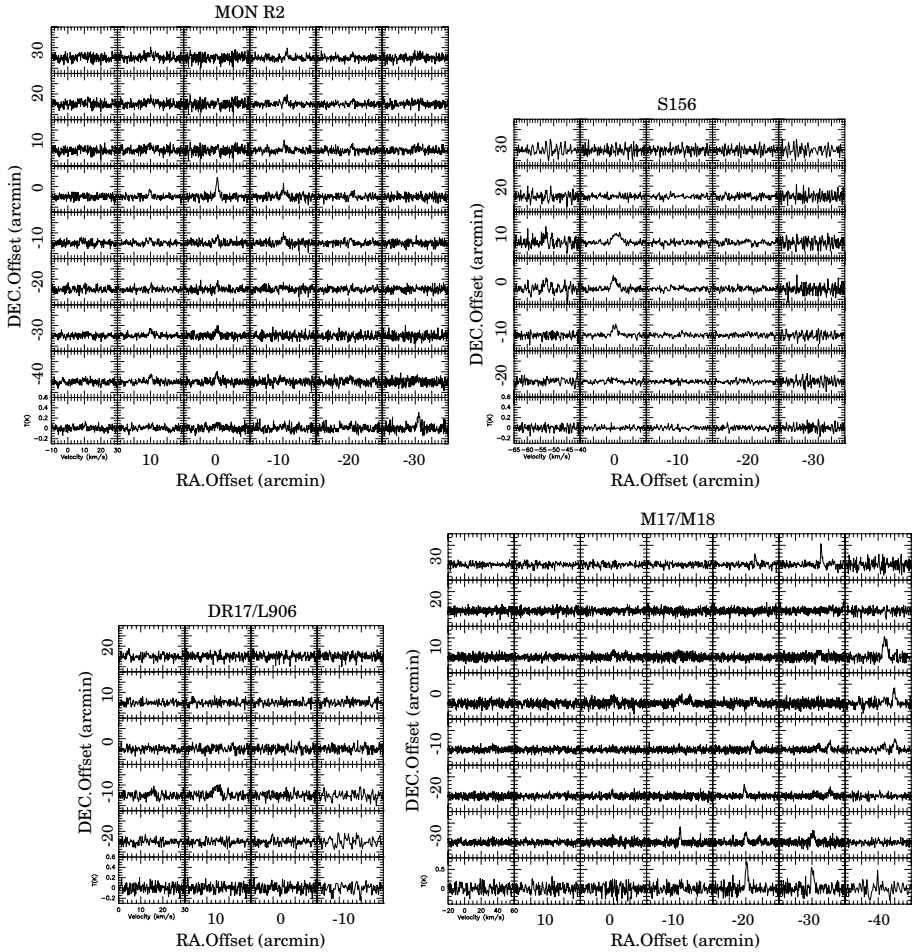

Fig. 2 The spectra of $C^{18}O$ (1–0) lines toward MON R2, S156, DR17/L906 and M17/M18 regions.

4.2 Comparison between H_2CO Absorption and $C^{18}O$ Emission

We compared the velocities of H_2CO and $C^{18}O$, and there is a good agreement between these two molecules towards the four regions that were studied (see Table B.1). The distributions of H_2CO and $C^{18}O$ towards these four regions are displayed as maps of integrated line intensities in Figure 1, which shows that H_2CO and $C^{18}O$ have quite a similar geometry and peak positions. The maximum in H_2CO absorption is located at the same position as the $C^{18}O$ peak, except for the DR17 region. The map shows that the extent of the H_2CO absorption is broader and smaller for the $C^{18}O$ emission in the four regions. This indicates that the two molecules are probing different parts of the molecular clouds. The $C^{18}O$ emission is more likely to be tracing denser gas than the H_2CO absorption. A total of 176 H_2CO absorption points were detected in four regions, but we only detected about 52 points with the $C^{18}O$ emission. The $C^{18}O$ is somewhat more difficult to detect than H_2CO. This may be because the density of the H_2CO absorption line is lower than that required to excite $C^{18}O$. A comparison between the mapping results of ^{12}CO and ^{13}CO towards the four regions (Tang et al. 2013) shows that the ranges for distributions of ^{12}CO, ^{13}CO, H_2CO and $C^{18}O$ are gradually

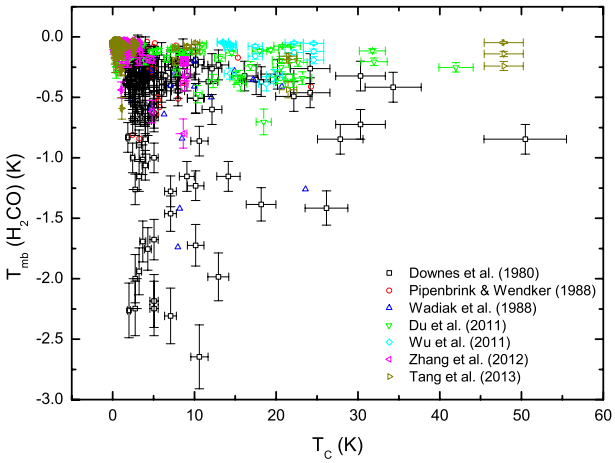

Fig. 3 The relation between the brightness temperature of H_2CO and background continuum.

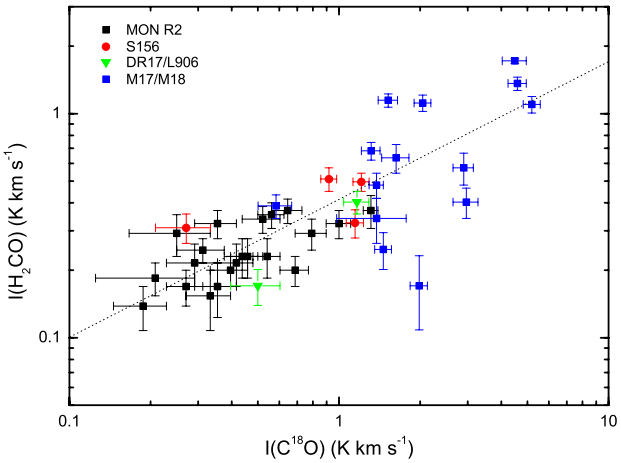

Fig. 4 Correlation between the H_2CO and $C^{18}O$ lines fluxes. The dashed line is the linear fit for H_2CO and $C^{18}O$ flux data.

decreasing. The correlation between the H_2CO and the ^{13}CO distributions is better than that between the H_2CO and ^{12}CO distributions and between the H_2CO and $C^{18}O$ distributions.

The relationship exhibited by fluxes between H_2CO and $C^{18}O$ has been investigated. We selected the data on fluxes that are shown as squares in Figure 4, and used them to make linear fits. The best linear fit to a straight line is,

$$\log \mathrm{I}(\mathrm{H_2CO}) = (0.60 \pm 0.06) \log \mathrm{I}(\mathrm{C^{18}O}) - (0.38 \pm 0.02)(\mathrm{K\ km\ s^{-1}}). \quad (1)$$

This shows that $I(H_2CO)$ is linearly well correlated with $I(C^{18}O)$, and the correlation coefficient is 0.8. Detections of the H_2CO absorption line depend on the brightness of the background continuum and the gas density. For the $C^{18}O$ lines, their intensities are dominated by the kinetic temperature of the gas. The fitted relation between $I(H_2CO)$ and $I(C^{18}O)$ indicates that the H_2CO absorption line can trace the dense, warm region of the molecular cloud.

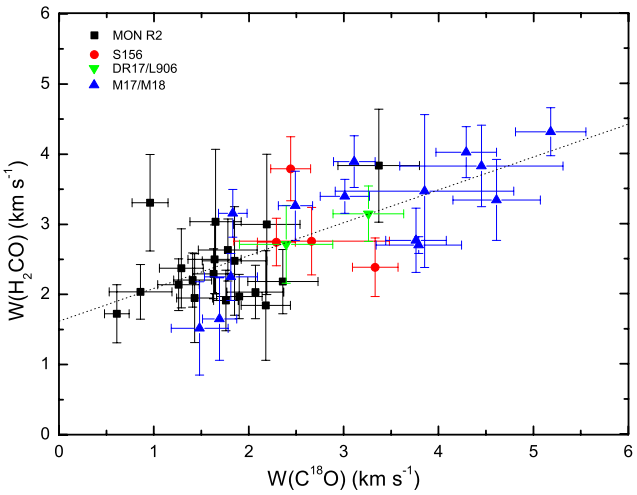

Fig. 5 The line widths of H_2CO and $C^{18}O$. The dashed line is the linear fit for H_2CO and $C^{18}O$ line widths, and the correlation coefficient is 0.7.

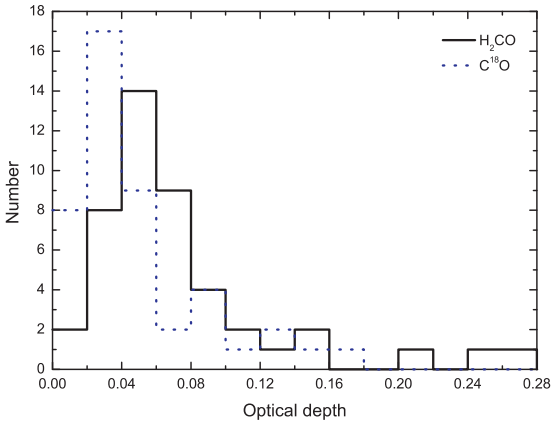

Fig. 6 The distribution of the peak optical depths of H_2CO and $C^{18}O$.

The line widths show the thermal motion and turbulence of internal kinematical properties of molecular clouds. H_2CO and $C^{18}O$ molecules have the same molecular weight, so the thermal line width is about 0.2 km s^{-1} for these two molecules, which is assumed to be at 30 K. All of the H_2CO and $C^{18}O$ line widths observed at a large scale exceed the thermal line width. In addition, the H_2CO line has components that show hyperfine structure. The contribution of hyperfine structure and thermal broadening to the measured H_2CO line widths is likely to be small to moderate (Tang et al. 2013). The correlations between the line widths of H_2CO and ^{12}CO and between those of H_2CO and ^{13}CO are not obvious in these four regions (Tang et al. 2013). A good correlation is shown towards the line widths between H_2CO and $C^{18}O$ (see Fig. 5). There is a similar range of line widths of 1 – 5 km s^{-1} for the two tracers. This indicates that the line broadening mechanism of the H_2CO and $C^{18}O$ lines could be similar in dense regions.

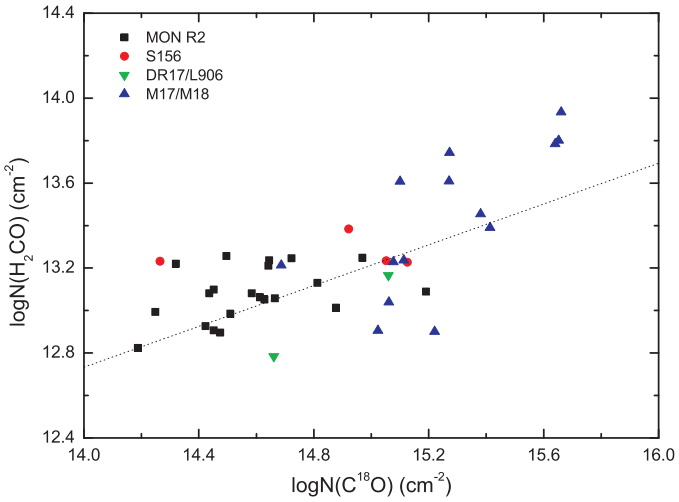

Fig. 7 Correlation of column densities for H_2CO and $C^{18}O$. The dotted line is the linear fit to the column densities for H_2CO and $C^{18}O$, and the correlation coefficient is 0.7.

The derived peak optical depths of H_2CO and $C^{18}O$ show that most of the optical depths for H_2CO are slightly higher than those of $C^{18}O$ (see Fig. 6). The average optical depth of H_2CO is $\langle\tau(H_2CO)\rangle \sim 0.05$ where $C^{18}O$ has also been detected. For $C^{18}O$, the average optical depth is $\langle\tau(C^{18}O)\rangle \sim 0.03$. Similar average optical depths of $C^{18}O$ and H_2CO indicate that the two tracers can both probe high density regions. The relationship between peak column densities of H_2CO and $C^{18}O$ shows that H_2CO has a rapid increase in abundance, but it is not as rapid as that of $C^{18}O$ (see Fig. 7). For the four regions, $N(H_2CO)$ is well correlated with $N(C^{18}O)$ and the average column density ratio is $\langle N(H_2CO)/N(C^{18}O)\rangle \sim 0.03$. The column density of H_2CO may be underestimated because the size of the cloud is smaller than our beam size. The true size of the cloud is overestimated (see e.g. Gardner & Whiteoak 1972; Slysh 1975), therefore the column density $N(H_2CO)$ may be higher than we estimated. At the same time, the column density of $C^{18}O$ could also be underestimated.

5 SUMMARY

We have carried out large scale $C^{18}O$ (1–0) mapping observations towards four Galactic HII regions using the 13.7 m radio telescope administered by Purple Mountain Observatory. The four regions, MON R2, S156, DR17/L906 and M17/M18, have been compared in terms of transitions of H_2CO (1_{10}–1_{11}), $C^{18}O$ (1–0) and the 6 cm continuum. A comparison of our study would be useful for the scientific community to investigate the molecular material associated with HII regions. The main conclusions of this study are as follows.

The distributions of H_2CO integrated intensity are similar to those of the 6 cm continuum towards the region of MON R2. This suggests that the H_2CO intensity is strongly influenced by the background continuum emission. In the S156 region, the H_2CO cloud might be affected by the HII region. The reason for similar H_2CO intensities towards the regions of DR17 and L906 could be that the continuum temperatures and the gas densities together influence the intensities of the H_2CO absorption line. Towards M17, there is a $10'$ offset between the H_2CO absorption and the intensity peaks for continuum emission.

Our analysis of the observed data and results of the Non–LTE model show that intensity of the H_2CO absorption line is not proportional to background continuum intensity when the continuum intensity is above about 10 K. The Non–LTE model shows that the brightness temperature of the H_2CO absorption line is strongest in a background continuum temperature range of about 3 – 8 K. The excitation of the H_2CO absorption line is affected by strong background continuum emissions. Approximately 75% of the observed positions with line-to-continuum ratio $|T_{\rm L}/T_{\rm C}|$ are less than 0.2 and the average value of $\langle|T_{\rm L}/T_{\rm C}|\rangle \sim 0.066$.

From our comparison of H_2CO and $C^{18}O$ maps, the extent of H_2CO absorption is found to be broader than that of $C^{18}O$ emission in the four regions. Except for the DR17 region, the maximum in H_2CO absorption is located at the same position as the $C^{18}O$ peak. The intensities and widths of H_2CO absorptions and $C^{18}O$ emission lines correlate fairly well. This indicates that the H_2CO absorption line can trace dense, warm regions of the molecular cloud. For the four regions, $N(H_2CO)$ is well correlated with $N(C^{18}O)$ and the average column density ratio is $\langle N(H_2CO)/N(C^{18}O)\rangle \sim 0.03$.

Acknowledgements We thank Zhi-Bo Jiang, Zhi-Wei Chen and Jun-Yu Li of Purple Mountain Observatory for providing the CO data of the M17/M18 region. We also thank Shu-Fei Yu for help with our English. This work was funded by the National Natural Science Foundation of China (Grant Nos. 10778703, 11373062, 11303081 and 10873025) and partly supported by the National Basic Research Program of China (973 program, 2012CB821800).

References

Bieging, J. H., Wilson, T. L., & Downes, D. 1982, A&AS, 49, 607
Dame, T. M., Elmegreen, B. G., Cohen, R. S., & Thaddeus, P. 1986, ApJ, 305, 892
Davis, C. J., Kumar, M. S. N., Sandell, G., et al. 2007, MNRAS, 374, 29
Downes, D., Wilson, T. L., Bieging, J., & Wink, J. 1980, A&AS, 40, 379
Downes, D., Winnberg, A., Goss, W. M., & Johansson, L. E. B. 1975, A&A, 44, 243
Federman, S. R., Huntress, W. T., Jr., & Prasad, S. S. 1990, ApJ, 354, 504
Fuller, G. A., Myers, P. C., Welch, W. J., et al. 1991, ApJ, 376, 135
Gardner, F. F., & Whiteoak, J. B. 1972, Astrophys. Lett., 12, 107
Gardner, F. F., Whiteoak, J. B., & Otrupcek, R. E. 1984, Proceedings of the Astronomical Society of Australia, 5, 557
Garrison, B. J., Lester, W. A., Jr., Miller, W. H., & Green, S. 1975, ApJ, 200, L175
Gilmore, W. 1980, AJ, 85, 912
Green, S., Garrison, B. J., Lester, W. A., Jr., & Miller, W. H. 1978, ApJS, 37, 321
Herbst, W., & Racine, R. 1976, AJ, 81, 840
Hoglund, B., & Gordon, M. A. 1973, ApJ, 182, 45
Israel, F. P. 1977, A&A, 59, 27
Lada, C., & Chaisson, E. J. 1975, ApJ, 195, 367
Lada, C. J. 1976, ApJS, 32, 603
Lindoff, U. 1971, A&A, 15, 439
Liszt, H., & Lucas, R. 1995, A&A, 299, 847
Liszt, H. S., Lucas, R., & Pety, J. 2006, A&A, 448, 253
McSwain, M. V., & Gies, D. R. 2005, ApJS, 161, 118
Mezger, P. G., & Henderson, A. P. 1967, ApJ, 147, 471
Minn, Y. K., Lee, H. K., & Greenberg, J. M. 1996, Journal of The Korean Astronomical Society, 29, S189
Pellegrini, E. W., Baldwin, J. A., Brogan, C. L., et al. 2007, ApJ, 658, 1119
Pipenbrink, A., & Wendker, H. J. 1988, A&A, 191, 313
Povich, M. S., Churchwell, E., Bieging, J. H., et al. 2009, ApJ, 696, 1278

Prasad, S. S., & Huntress, W. T., Jr. 1980, ApJ, 239, 151
Racine, R. 1968, AJ, 73, 233
Ridge, N. A., Wilson, T. L., Megeath, S. T., Allen, L. E., & Myers, P. C. 2003, AJ, 126, 286
Rodríguez, M. I., Wiklind, T., Allen, R. J., Escalante, V., & Loinard, L. 2007, ApJ, 663, 824
Sato, F., Mizuno, A., Nagahama, T., et al. 1994, ApJ, 435, 279
Schneider, N., Bontemps, S., Simon, R., et al. 2006, A&A, 458, 855
Scoville, N. Z., Solomon, P. M., & Thaddeus, P. 1972, ApJ, 172, 335
Slysh, V. I. 1975, Soviet Ast., 18, 405
Snyder, L. E., Buhl, D., Zuckerman, B., & Palmer, P. 1969, Physical Review Letters, 22, 679
Tang, X. D., Esimbek, J., Zhou, J. J., et al. 2013, A&A, 551, A28
Troscompt, N., Faure, A., Maret, S., et al. 2009, A&A, 506, 1243
Tsivilev, A. P., & Krasnov, V. V. 1999, Astronomy Reports, 43, 511
van den Bergh, S. 1966, AJ, 71, 990
van der Tak, F. F. S., Black, J. H., Schöier, F. L., Jansen, D. J., & van Dishoeck, E. F. 2007, A&A, 468, 627
Wendker, H. J. 1984, A&AS, 58, 291
Whiteoak, J. B., & Gardner, F. F. 1974, A&A, 37, 389
Wood, D. O. S., & Churchwell, E. 1989, ApJS, 69, 831
Wootten, A., Snell, R., & Evans, N. J., II 1980, ApJ, 240, 532
Young, K. E., Lee, J.-E., Evans, N. J., II, Goldsmith, P. F., & Doty, S. D. 2004, ApJ, 614, 252
Zhang, C. P., Esimbek, J., Zhou, J. J., Wu, G., & Du, Z. M. 2012, Ap&SS, 337, 283

Appendix A: THE NON-LTE MODEL FOR H_2CO

The model is based on statistical equilibrium calculations that involve collisional and radiative processes and include radiation from background sources, and the effects of optical depth are treated with an escape probability method. The Non–LTE model was generated by assuming that the hydrogen density $n(H_2) = 10^4$ cm^{-3} (Garrison et al. 1975; Green et al. 1978; Rodríguez et al. 2007; Troscompt et al. 2009), H_2CO column density $N(H_2CO) = 1.0\times10^{13}$, 5.0×10^{13} and 1.0×10^{14} cm^{-2} (Federman et al. 1990; Troscompt et al. 2009; Tang et al. 2013), H_2CO line width FWHM ΔV (H_2CO) = 2.5 km s^{-1} (Pipenbrink & Wendker 1988; Tang et al. 2013) and the range of kinetic temperatures T_k is 10 – 40 K.

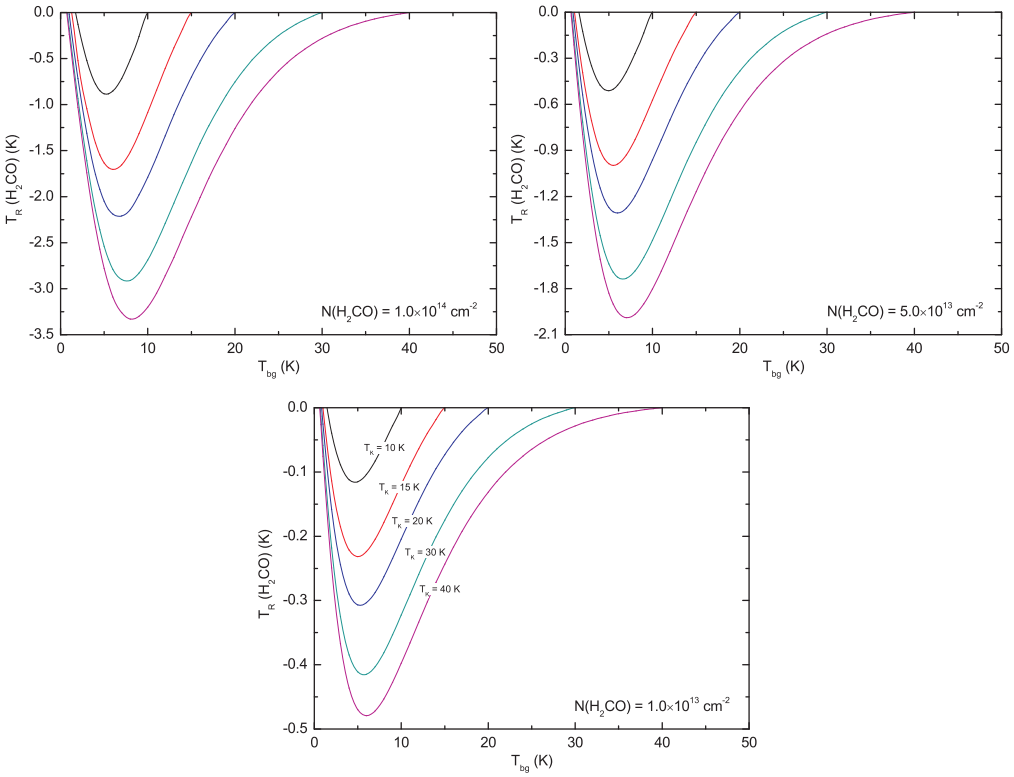

Fig. A.1 Brightness temperature of H_2CO vs. background continuum for different kinetic temperatures T_k. The plot was generated assuming hydrogen density $n(H_2) = 10^4$ cm^{-3}; H_2CO column density $N(H_2CO) = 1.0 \times 10^{13}$, 5.0×10^{13}, and 1.0×10^{14} cm^{-2}; line width FWHM ΔV (H_2CO) = 2.5 km s^{-1} and kinetic temperatures T_k = 10, 15, 20, 30 and 40 K, using the code for the Non-LTE model of interstellar line spectra (van der Tak et al. 2007).

Appendix B: THE LINE PARAMETERS AND SPECTRA OF $C^{18}O$

Table B.1: The parameters of $C^{18}O$(1–0) and H_2CO (1_{10}–1_{11})

Sources	Offset (arcmin)	I($C^{18}O$) (K km s^{-1})	Velocity (km s^{-1})	Width (km s^{-1})	T_A^* (K)	I(H_2CO) (K km s^{-1})	Velocity (km s^{-1})	Included in fits
MON R2	0, 0					−0.30 (0.04)	7.6 (0.2)	
		0.63 (0.04)	10.4 (0.1)	1.76 (0.13)	0.34	−0.24 (0.04)	10.5 (0.1)	Y
	−10, 0	0.48 (0.05)	10.7 (0.2)	3.37 (0.43)	0.13	−0.21 (0.03)	10.7 (0.3)	Y
	−10, −10	0.33 (0.04)	10.5 (0.2)	2.36 (0.37)	0.13	−0.13 (0.02)	10.6 (0.2)	Y
	0, −10	0.22 (0.03)	10.4 (0.1)	1.64 (0.28)	0.12	−0.15 (0.03)	9.7 (0.3)	Y
	10, −10	<0.16				−0.08 (0.02)	9.3 (0.1)	
	10, 0	0.21 (0.03)	9.7 (0.1)	1.43 (0.19)	0.14	−0.15 (0.03)	9.1 (0.2)	Y
	10, 10	<0.06				−0.05 (0.02)	9.9 (0.2)	
	0, 10	<0.08				−0.09 (0.02)	10.5 (0.1)	
	−10, 10	0.17 (0.03)	10.7 (0.1)	0.96 (0.19)	0.16	−0.21 (0.03)	10.7 (0.3)	Y
	−20, 10	0.17 (0.03)	11.8 (0.2)	1.65 (0.27)	0.10	−0.11 (0.03)	11.9 (0.5)	Y
	−20, 0	0.14 (0.03)	12.1 (0.3)	2.19 (0.35)	0.06	−0.14 (0.03)	11.6 (0.4)	Y
	−20, −10	0.13 (0.02)	11.1 (0.1)	1.29 (0.23)	0.10	−0.11 (0.02)	10.9 (0.3)	Y
	−20, −20	<0.05				...		
	−10, −20	<0.09				−0.09 (0.03)	10.1 (0.6)	
	0, −20	0.15 (0.03)	10.2 (0.1)	1.33 (0.32)	0.11	−0.16 (0.02)	9.1 (0.1)	Y
	10, −20	0.09 (0.02)	10.4 (0.1)	0.61 (0.13)	0.14	−0.09 (0.02)	10.0 (0.3)	Y
	20, −20	<0.03				−0.12 (0.03)	9.8 (0.3)	
	20, −10	<0.07				−0.09 (0.03)	9.2 (0.4)	
	20, 0	<0.04				−0.08 (0.02)	9.0 (0.3)	
	20, 10	<0.09				...		
	20, 20	<0.05				...		
	10, 20	<0.10				...		
	0, 20	0.10 (0.04)	10.7 (0.2)	0.86 (0.33)	0.11	−0.12 (0.02)	9.9 (0.2)	Y
	−10, 20	0.20 (0.03)	11.7 (0.2)	2.18 (0.26)	0.09	−0.14 (0.03)	11.1 (0.2)	Y
	−20, 20	0.16 (0.03)	12.4 (0.2)	1.85 (0.34)	0.08	−0.10 (0.03)	12.0 (0.4)	Y
	−30, 20	<0.08				...		
	−30, 10	<0.09				−0.07 (0.03)	13.6 (0.4)	
	−30, 0	<0.04				−0.10 (0.02)	11.9 (0.2)	
	−30, −10	<0.10				−0.21 (0.03)	11.8 (0.3)	
	−30, −20	<0.09				−0.10 (0.03)	8.5 (0.4)	
	−30, −30	...				−0.14 (0.05)	9.2 (0.5)	
	−20, −30	...				−0.07 (0.03)	9.8 (0.4)	
	−10, −30	...				−0.09 (0.04)	9.5 (0.9)	
	0, −30	0.25 (0.04)	10.5 (0.1)	1.78 (0.31)	0.13	−0.22 (0.03)	8.9 (0.2)	Y
	10, −30	0.27 (0.03)	10.1 (0.1)	2.07 (0.30)	0.12	−0.23 (0.03)	9.6 (0.1)	Y
	20, −30	<0.01				−0.11 (0.03)	8.9 (0.3)	
	20, 30	<0.07				−0.14 (0.05)	9.6 (0.6)	
	10, 30	<0.12				−0.19 (0.04)	10.0 (0.4)	
	0, 30	...				−0.08 (0.02)	10.1 (0.3)	
	−10, 30	0.19 (0.03)	12.4 (0.1)	1.26 (0.22)	0.14	−0.13 (0.02)	11.9 (0.1)	Y
	−20, 30	0.10 (0.03)	12.2 (0.2)	1.40 (0.36)	0.07	...		
	−30, 30	<0.10				...		
	−30, −40	<0.07				−0.12 (0.03)	11.8 (0.3)	
	−20, −40	<0.05				−0.05 (0.02)	12.4 (0.5)	
	−10, −40	<0.06				−0.09 (0.02)	8.4 (0.4)	
	0, −40	0.31 (0.04)	10.1 (0.1)	1.63 (0.22)	0.18	−0.24 (0.03)	9.3 (0.1)	Y
	10, −40	0.26 (0.03)	10.1 (0.1)	1.90 (0.24)	0.13	−0.15 (0.03)	9.9 (0.2)	Y
	20, −40	<0.05				−0.11 (0.04)	9.2 (0.2)	
	−30, −50	0.38 (0.05)	12.2 (0.1)	1.41 (0.20)	0.26	−0.19 (0.03)	12.1 (0.2)	Y
	−20, −50	<0.04				...		
	−10, −50	<0.11				...		
	0, −50	...				...		
	10, −50	...				−0.07 (0.03)	10.3 (0.4)	

Table B.1: continued.

Source	Offset (arcmin)	I($C^{18}O$) (K km s^{-1})	Velocity (km s^{-1})	Width (km s^{-1})	T_A^* (K)	I(H_2CO) (K km s^{-1})	Velocity (km s^{-1})	Included in fits
	20, −50	0.08 (0.02)	10.7 (0.1)	0.84 (0.23)	0.09	...		
S156	0, 0	0.58 (0.04)	−52.1 (0.1)	2.44 (0.21)	0.23	−0.32 (0.03)	−50.2 (0.2)	Y
	−10, 0	<0.04				−0.09 (0.02)	−49.0 (0.3)	
	−10, −10	<0.05				−0.13 (0.03)	−48.7 (0.4)	
	0, −10	0.44 (0.03)	−51.9 (0.1)	2.29 (0.20)	0.18	−0.33 (0.04)	−50.2 (0.2)	Y
	10, −10	...				...		
	10, 0	0.25 (0.06)	−53.0 (0.2)	1.43 (0.45)	0.16	...		
	10, 10	0.23 (0.07)	−53.0 (0.2)	1.20 (0.58)	0.18	−0.09 (0.03)	−50.1 (0.2)	
	0, 10	0.55 (0.04)	−51.1 (0.1)	3.33 (0.24)	0.15	−0.21 (0.03)	−50.2 (0.2)	Y
	−10, 10	<0.02				−0.08 (0.02)	−49.0 (0.3)	
	−20, 10	<0.02				−0.05 (0.02)	−45.0 (0.4)	
	−20, 0	...				...		
	−20, −10	<0.08				...		
	−20, −20	<0.03				...		
	−10, −20	...				−0.12 (0.04)	−49.5 (0.6)	
	0, −20	0.13 (0.03)	−52.2 (0.4)	2.66 (0.82)	0.04	−0.20 (0.03)	−49.4 (0.2)	Y
	10, −20	<0.05				−0.09 (0.03)	−50.6 (0.5)	
	10, 20	<0.01				−0.08 (0.03)	−50.4 (0.4)	
	0, 20	<0.02				−0.07 (0.02)	−49.1 (0.3)	
	−10, 20	<0.03				−0.13 (0.03)	−50.3 (0.4)	
	−20, 20	<0.01				−0.10 (0.04)	−51.1 (0.7)	
	−30, 20	...				...		
	−30, 10	<0.03				−0.08 (0.02)	−50.2 (0.4)	
	−30, 0	<0.02				...		
	−30, −10	<0.01				−0.09 (0.04)	−46.8 (0.9)	
	−30, −20	<0.04				...		
	−30, −30	<0.02				−0.08 (0.03)	−54.3 (0.4)	
	−20, −30	<0.02				...		
	−10, −30	...				...		
	0, −30	...				...		
	10, −30	<0.01				...		
	10, 30	<0.03				...		
	0, 30	<0.04				...		
	−10, 30	<0.02				...		
	−20, 30	<0.04				...		
	−30, 30	<0.04				...		
DR17/L906	0, 0	<0.05				−0.37 (0.05)	7.0 (0.2)	
	−10, 0	<0.04				−0.11 (0.02)	5.8 (0.3)	
	−10, −10	...				−0.09 (0.03)	7.7 (0.5)	
	0, −10	<0.01				−0.06 (0.03)	6.9 (0.3)	
						−0.09 (0.03)	9.8 (0.5)	
	10, −10					−0.10 (0.02)	7.1 (0.2)	
		0.56 (0.06)	14.4 (0.2)	3.26 (0.34)	0.16	−0.26 (0.03)	15.4 (0.2)	Y
	10, 0	<0.11				−0.14 (0.02)	6.5 (0.2)	
	10, 10	<0.05				−0.07 (0.01)	6.6 (0.2)	
	0, 10	<0.04				−0.23 (0.03)	6.2 (0.3)	
						−0.05 (0.02)	14.7 (0.4)	
	−10, 10	...				−0.07 (0.02)	6.8 (0.3)	
	−10, −20	...				−0.06 (0.03)	5.9 (0.5)	
	0, −20	<0.01				−0.06 (0.02)	6.4 (0.3)	
						−0.05 (0.02)	10.7 (0.4)	
	10, −20	<0.06				−0.12 (0.02)	6.5 (0.2)	
	20, −20	<0.09				−0.22 (0.03)	4.6 (0.2)	
						−0.07 (0.02)	14.0 (0.1)	
	20, −10					−0.05 (0.02)	4.6 (0.4)	
		0.24 (0.05)	15.3 (0.3)	2.40 (0.49)	0.10	−0.11 (0.02)	15.8 (0.2)	Y
	20, 0	<0.03				...		

Table B.1: continued.

Source	Offset (arcmin)	I($C^{18}O$) (K km s^{-1})	Velocity (km s^{-1})	Width (km s^{-1})	T_A^* (K)	I(H_2CO) (K km s^{-1})	Velocity (km s^{-1})	Included in fits
	20, 10	<0.02				...		
	20, 20	...				...		
	10, 20	<0.06				−0.11 (0.03)	5.7 (0.6)	
	0, 20	<0.02				−0.08 (0.04)	9.7 (0.4)	
	−10, 20	<0.02				−0.09 (0.04)	7.5 (0.7)	
	−10, −30	...				...		
	0, −30	<0.06				−0.05 (0.02)	5.4 (0.2)	
	10, −30	<0.04				−0.09 (0.02)	7.4 (0.2)	
	20, −30	<0.05				−0.25 (0.01)	6.6 (0.3)	
						−0.05 (0.02)	14.0 (0.1)	
M17/M18	0, 0					−0.17 (0.04)	16.6 (0.1)	
		<0.75				−0.36 (0.04)	22.2 (0.1)	
						−0.08 (0.04)	38.1 (0.6)	
	−10, 0					−0.49 (0.06)	15.0 (1.2)	
						−0.43 (0.06)	19.2 (1.2)	
		0.78 (0.09)	20.6 (0.3)	6.19 (0.88)	0.12	−0.41 (0.06)	22.4 (1.2)	Y
		0.69 (0.08)	31.5 (0.4)	5.74 (0.80)	0.11			
	−10, −10	<0.12				−0.32 (0.04)	18.7 (0.4)	
						−0.06 (0.03)	26.2 (0.2)	
	0, −10	<0.19				−0.10 (0.05)	18.4 (0.5)	
						−0.10 (0.03)	21.2 (0.1)	
	10, −10	<0.37				...		
	10, 0	<0.15				...		
	10, 10	<0.22				−0.05 (0.05)	20.9 (1.2)	
						−0.06 (0.05)	22.7 (0.5)	
	0, 10					−0.24 (0.05)	17.8 (0.4)	
		<0.56				−0.13 (0.04)	22.3 (0.4)	
		0.33 (0.07)	34.7 (0.5)	4.41 (1.04)	0.07			
	−10, 10	<0.51				−0.54 (0.06)	17.5 (0.2)	
						−0.10 (0.04)	21.9 (0.4)	
	−20, 10	...				−0.06 (0.02)	39.3 (0.2)	
	−20, 0	<0.24				−0.10 (0.02)	30.2 (0.2)	
	−20, −10					−0.07 (0.04)	18.1 (1.1)	
		0.63 (0.06)	28.5 (0.2)	3.53 (0.37)	0.17			
	−20, −20	0.66 (0.04)	18.5 (0.1)	2.49 (0.18)	0.25	−0.31 (0.04)	17.6 (0.2)	Y
						−0.07 (0.03)	28.4 (0.5)	
						−0.08 (0.04)	37.0 (0.5)	
	−10, −20	...				−0.07 (0.02)	18.1 (0.3)	
	0, −20	0.28 (0.04)	18.6 (0.1)	1.81 (0.28)	0.15	−0.25 (0.03)	17.7 (0.1)	Y
						−0.05 (0.02)	32.2 (0.2)	
	10, −20	<0.17				−0.06 (0.02)	19.2 (0.3)	
	20, −20	<0.04				−0.03 (0.03)	21.8 (0.8)	
						−0.13 (0.06)	37.8 (1.3)	
	20, −10	<0.27				−0.06 (0.04)	15.5 (0.7)	
	20, 0	<0.23				...		
	20, 10	<0.15				...		
	20, 20	<0.15				...		
	10, 20	<0.12				−0.09 (0.03)	21.5 (0.6)	
	0, 20	<0.12				−0.16 (0.04)	19.9 (0.8)	
	−10, 20	...				−0.07 (0.02)	20.0 (0.1)	
	−20, 20	...				−0.11 (0.03)	21.3 (0.1)	
						−0.05 (0.02)	29.4 (0.4)	
	−30, 20	<0.40				−0.07 (0.03)	29.2 (0.6)	
	−30, 10	<0.19				−0.05 (0.03)	39.3 (0.3)	
	−30, 0	<0.15				−0.05 (0.02)	22.0 (0.3)	
	−30, −10					−0.06 (0.02)	23.7 (0.1)	
						−0.07 (0.02)	27.3 (0.2)	

Table B.1: continued.

Source	Offset (arcmin)	I($C^{18}O$) (K km s^{-1})	Velocity (km s^{-1})	Width (km s^{-1})	T_A^* (K)	I(H_2CO) (K km s^{-1})	Velocity (km s^{-1})	Included in fits
		0.70 (0.05)	41.2 (0.1)	3.76 (0.32)	0.17	−0.16 (0.03)	39.1 (0.2)	Y
	−30, −20					−0.06 (0.02)	16.9 (0.2)	
						−0.15 (0.03)	20.7 (0.3)	
		0.70 (0.06)	41.8 (0.2)	5.37 (0.53)	0.12			
	−30, −30	0.98 (0.07)	21.1 (0.2)	4.29 (0.32)	0.22	−0.72 (0.06)	18.2 (0.2)	Y
						−0.10 (0.05)	32.6 (0.9)	
	−20, −30	0.73 (0.06)	20.1 (0.1)	3.11 (0.22)	0.28	−0.74 (0.05)	18.6 (0.1)	Y
						−0.06 (0.03)	34.9 (0.6)	
	−10, −30	0.63 (0.05)	20.6 (0.1)	1.83 (0.15)	0.33	−0.44 (0.04)	18.7 (0.1)	Y
						−0.11 (0.04)	35.4 (0.6)	
	0, −30	<0.34				−0.24 (0.06)	16.8 (0.6)	
						−0.05 (0.04)	34.2 (1.2)	
	10, −30	<0.09				−0.08 (0.04)	19.6 (0.3)	
						−0.07 (0.04)	34.4 (0.4)	
	20, −30	<0.22				−0.05 (0.03)	37.2 (1.0)	
	20, 30	<0.06				...		
	10, 30	<0.07				−0.09 (0.05)	28.9 (0.9)	
	0, 30	...				...		
	−10, 30	<0.06				...		
	−20, 30	0.55 (0.07)	31.4 (0.1)	1.86 (0.30)	0.28	...		
	−30, 30					−0.08 (0.03)	23.4 (0.3)	
		0.95 (0.07)	31.1 (0.1)	1.69 (0.18)	0.53	−0.11 (0.04)	28.1 (0.4)	Y
						−0.06 (0.04)	38.3 (0.3)	
	−40, 30	...				−0.14 (0.05)	26.9 (0.4)	
	−40, 20	<0.05				−0.16 (0.07)	27.5 (1.3)	
	−40, 10	2.49 (0.18)	28.3 (0.2)	5.18 (0.37)	0.45	−0.71 (0.06)	25.4 (0.2)	Y
	−40, 0					−0.11 (0.04)	26.3 (0.2)	
		1.42 (0.15)	39.5 (0.2)	3.49 (0.48)	0.38	−0.26 (0.04)	36.9 (0.1)	Y
	−40, −10	1.39 (0.12)	40.5 (0.2)	4.61 (0.46)	0.28	−0.37 (0.06)	37.8 (0.3)	Y
	−40, −20	<0.19				−0.10 (0.04)	18.9 (0.2)	
						−0.08 (0.05)	23.9 (0.9)	
						−0.22 (0.08)	35.3 (0.8)	
	−40, −30	<0.15				−0.11 (0.04)	34.0 (0.6)	
	−40, −40	<0.12				−0.62 (0.07)	18.3 (0.2)	
						−0.12 (0.06)	32.6 (1.0)	
	−30, −40	2.15 (0.22)	20.7 (0.2)	3.79 (0.45)	0.53	−1.11 (0.03)	18.5 (0.1)	Y
						−0.08 (0.04)	36.8 (0.3)	
	−20, −40	2.20 (0.17)	21.2 (0.1)	3.01 (0.26)	0.69	−0.88 (0.06)	18.7 (0.1)	Y
						−0.05 (0.03)	36.5 (0.6)	
	−10, −40	0.66 (0.19)	21.8 (0.6)	3.85 (0.94)	0.16	−0.22 (0.05)	18.3 (0.4)	Y
						−0.09 (0.04)	37.1 (0.7)	
	0, −40	...				−0.06 (0.03)	18.6 (0.6)	
	10, −40	...				−0.23 (0.06)	26.2 (0.1)	
	20, −40	<0.10				...		

Notes: The coordinates of the four regions are MON R2 ($06^h07^m46.60^s$, $-06°22'59.0''$, J2000.0) (Herbst & Racine 1976), S156 ($23^h05^m24.80^s$, $60°08'14.0''$) (Hoglund & Gordon 1973), DR17/L906 ($20^h35^m06.16^s$, $42°20'23.7''$) (Schneider et al. 2006) and M17/M18 ($18^h20^m47.11^s$, $-16°10'17.5''$) (Downes et al. 1980). "..." indicates that the corresponding spectra could not be detected or data were not available so no reliable fit could be made. H_2CO data were selected from Tang et al. (2013). Values marked with "Y" are plotted as squares in Figure 4 and the data have been converted from the antenna temperature to the brightness temperature of the line.